Enhanced strength-ductility synergy in a Mo and W co-doping NiCoCr multi-principal element alloy at ambient and cryogenic temperatures

Junchen Liu [a], Chenliang Chu [a], Yemao Lu [b], Zhao Tian [a], Weiping Chen [a], Zhiqiang Fu [a,*]

[a] Guangdong Key Laboratory for Advanced Metallic Materials Processing, South China University of Technology, Guangzhou, Guangdong, 510641, China
[b] Institute of Nanotechnology, Karlsruhe Institute of Technology (KIT), D-76021, Karlsruhe, Germany

Keywords:
Multi-principal element alloys
Mechanical properties
Strengthening mechanisms
Deformation mechanisms
Cryogenic temperatures

A B S T R A C T

A novel designed $Ni_{48}Co_{33}Cr_9Mo_4W_6$ multi-principal element alloy (MPEA) with single face-centered cubic (FCC) solid-solution phase was fabricated by casting, homogenization, cold rolling, and various post deformation annealing (PDA) heat treatments. The single-phase FCC structured samples with homogeneous grains exhibited average grain sizes ranging from ~1.4 to ~47.8 μm. In addition, a single-phase FCC structured heterogeneous sample consisting of partially un-recrystallized region (~47.1 vol%) and fully recrystallized region (~52.9 vol%) was also achieved. Among all the samples with homogeneous grains, the sample processed using PDA treatment at 900 °C for 3 min (named as PDA900-3min) showed an average grain size of ~1.4 μm, displaying the best mechanical properties. In detail, it exhibited a yield strength of ~811 MPa and a total elongation of ~40.2 % at ambient temperature (298 K), and these values were increased to ~1085 MPa and ~42.7 % at LN_2 (77 K) temperature. Due to heterogeneous deformation induced (HDI) strengthening, the hetero-structured sample (named as PDA900-90s) present markedly higher strength and slightly lower ductility in comparison with the PDA900-3min sample at 298 K and 77 K. These two samples demonstrated synergetic improvement of strength and ductility through Mo/W co-doping and PDA heat treatments both at ambient and LN_2 temperatures, attributing to solid solution strengthening and grain boundary strengthening, as well as heterogeneous deformation induced (HDI) strengthening. Additionally, Mo/W co-doping, reduces the stacking fault energy (SFE) of the alloy, facilitates the generation of stacking faults (SFs) and twins, which is prone to maintaining the higher work hardening rate. Therefore, our work suggests that Mo and W co-doping is an effective strategy for achieving enhanced strength-ductility synergy in FCC structured MPEAs.

1. Introduction

Recently, multi-principal element alloys (MPEAs) have garnered considerable attention from researchers due to their remarkable mechanical properties, which can be achieved through careful regulation of composition and utilization of various processing methods [1–4]. Among the reported MPEAs, those with face-center cubic (FCC) structures provide broad range of opportunities to achieve the synergetic enhancement of strength and ductility [5–8], in comparison with the ones with body-center cubic (BCC) and hexagonal close-packed (HCP) structures. However, relatively low yield strength of FCC MPEAs limits their engineering applications.

To enhance the strength of FCC MPEAs, several approaches have been exploited. The typical strengthening mechanisms provide diversified methods for strengthening FCC structured alloys, including introduction of nano-sized precipitates, solid solution strengthening induced by doping minor other elements, and grain boundary strengthening [9–11]. In terms of single-phase FCC alloys, solid solution strengthening and grain boundary strengthening are typically applied simultaneously. He et al. [12] reported that minor additions of Al and Ti elements to the $Ni_2CoCrFe$ matrix induced an increased degree of short-range ordering (SRO), enhancing the resistance to dislocation motion, leading to excellent work-hardening ability. Accordingly, enhanced strength and ductility were obtained. Additionally, Li et al. [13] utilized a misfit-volume-maximization strategy to improve ultimate tensile strength without significant sacrifice in ductility. As such, the binary single-phase FCC structured Ni–Mo_{20} alloy was designed with superb strength (1.05 GPa) and good ductility (37 %) by restricting the motion of dislocation through volume misfit and grain boundary. Nevertheless, it should be noted that the excessive addition of solute

* Corresponding author.
E-mail address: zhiqiangfu2019@scut.edu.cn (Z. Fu).

atoms may lead to the formation of undesired precipitates, which can significantly reduce ductility [14,15]. Additionally, noticeable reduction in ductility often occurs when the grain size of alloys refined to lower than 1 μm [16].

A phenomenon known as heterogeneous deformation induced (HDI) strengthening [17,18], has been accepted that heterogeneous structure could lead to higher strength with acceptable ductility [19]. Typically, dual-phase structured alloys possess outstanding strengths attributed to the hetero-deformation of the soft and hard phases. Jiang et al. [2] constructed a fibrous heterogeneous structure through casting, displaying fibers-like FCC phase which was wrapped with shell-like ordered BCC phase. With a true strain of 3.5 %, a high-density dislocation was detected in the fiber-like FCC phase and FCC/B2 interface, confirming the HDI strengthening effect during the deformation process. Additionally, HCP phases can also serve as hard phases to impede the motion of dislocation within the soft FCC matrix. Zhou et al. [20] achieved synergetic improvement of strength and elongation in the $Fe_{50}Mn_{30}Co_{10}Cr_{10}$ HEA through ultra-fast annealing-deep cryogenic treatment-tempering method. The nano-scale needle-like HCP phase formed during the deep cryogenic treatment contributed to the higher strength without sacrificing ductility. For single-phase FCC alloys, the uncrystallized region with severe residual stress, and the region with finer grain size and higher strength can also play a similar role during deformation as the hard phase mentioned above. Slone et al. [21] explored the influence of residual deformation structure and multi-modal grain size distribution on the strength of CrCoNi alloy, confirming that partially recrystallized region acted as hard inclusions during deformation. Therefore, the HDI strengthening induced by inhomogeneous deformation leaded to better mechanical properties compared to the sole grain boundary strengthening. Meanwhile, several studies have shown that the combination of heterogeneous structure, solid solution strengthening and grain boundary strengthening is an effective method to enhance the strength-ductility synergy in single-phase FCC alloys [22,23]. In addition, as is known to all, FCC alloys, usually possess appealing mechanical properties at cryogenic temperatures due to the conjugated mechanisms of planar slip, stacking faults, and deformation-induced twinning [24–28]. Unfortunately, there have been few reports on the differences in strengthening and deformation mechanisms between heterogeneous and homogeneous structured FCC MPEAs at both cryogenic and ambient temperatures [29], and therefore the underlying mechanisms remains unclearly.

Therefore, on the basis of the above-mentioned discussion, we designed a novel $Ni_{48}Co_{33}Cr_9Mo_4W_6$ MPEA based on the equi-atomic CoCrNi MPEA [30]. In detail, the concentration of Ni element was creased to realize higher solubility of Mo and W elements, which would be in favor of achieving a proper combination of solid solution strengthening and grain boundary strengthening. The addition of Mo and W elements can also reduce stacking fault energy (SFE) of the alloy [31,32], which would facilitate the occurrence of annealing twins, stacking faults (SFs) and deformation twins (DTs), giving rise to achieve a higher work hardening rate. The $Ni_{48}Co_{33}Cr_9Mo_4W_6$ MPEA was first prepared by casting, homogenization, and PDA heat treatments. Finally, various grain sizes were achieved in the homogeneous structured samples, and a heterogeneous structured sample comprising partially un-recrystallized region and fully recrystallized grains was also obtained. Mechanical tests and microstructural characterizations have been employed to understand the influence of temperature on the strengthening and deformation mechanisms between heterogeneous-structured and homogeneous-structured samples, ultimately achieving synergistic improvements in strength and ductility.

2. Methods

2.1. Materials

The cast ingots in this work were fabricated by electric arc-melting under the high purity argon atmosphere with the nominal composition of $Ni_{48}Co_{33}Cr_9Mo_4W_6$, then these ingots were processed into cubic with the dimension of 60 × 30 × 7.5 mm^3 by electric discharged machine (EDM). The as-cast samples were homogenized at 1200 °C for 6 h in a tubular heat treatment furnace under a flowing argon gas environment (denoted as Homo). After cold rolling process with a 80 % total reduction (from 7.5 to 1.5 mm), the sample was annealed through an electric-resistant furnace at 900 °C for 90 s, 3 min, 15 min, at 950 °C, 975 °C, 1000 °C, 1100 °C, 1200 °C for 15 min, at 1200 °C for 1 h, which defined as PDA900-90s, PDA900-3min, PDA900-15min, PDA950-15mn, PDA975-15min, PDA1000-15min, PDA1200-15min and PDA1200-1h, respectively. The calculation of phase diagram (CALPHAD) was conducted by Thermo-Calc using the TECH6 database.

2.2. Tensile test

The flat dog-bone-shaped specimens used for tensile test were fabricated by EDM with a gauge length of 10 mm, a width of 3 mm, and the thickness is 1.2 mm. All samples were polished with SiC abrasive paper from 180# to 2000# to remove the surface defects. These tensile tests at ambient temperature (298 K) and cryogenic temperature (77 K) were conducted by universal testing machine (MTS) with the strain rate of 10^{-3} s^{-1} under the control of a mechanical extensometer. Three samples for each test were prepared to ensure data accuracy.

2.3. Microstructure characterization

The phase constitution was identified by X-ray diffraction (XRD) with Cu K_α radiation at the speed of 6°/min from 20° to 100°. The back-scattered electron images (BSE) were conducted by Phenom X1, and the microstructure evolution was investigated through electron back-scattered diffraction (EBSD) and electron channeling contrast imaging (ECCI) equipped on a field emission scanning electron microscope (FE-SEM). Detailed microstructures were explored by transmission electron microscopy (TEM) coupled with energy dispersive X-ray spectroscopy (EDS). The samples used for BSE, EBSD, and ECCI were prepared by electrochemical polished with a solution ($HClO_4$:C_2H_6O = 1:9 vol%) at 298 K with the voltage of 24 V. And the thin foils needed by TEM were grid to 80 μm by 2000# SiC abrasive paper. Subsequently, an automatic twin-jet electro-polisher and ion-polishing system (PIPS, Gatan 695) were applied to get required samples.

3. Results

3.1. Phase constitutions

XRD and CALPHAD analyses were carried out to confirm the existence of single FCC phase in the $Ni_{48}Co_{33}Cr_9Mo_4W_6$ MPEA samples. The XRD patterns of the selected samples are shown in Fig. 1(a). The 2θ degree of diffraction peaks correspond to the FCC structure, and their primary diffraction peaks are (111) plane. In addition, the XRD patterns also indicate that the phase constitution is identical among different samples. The lattice constant of the studied MPEA is measured to be ~3.592 Å based on the XRD patterns.

Additionally, the phase diagram of the studied MPEA is provided in Fig. 1(b). Clearly, the MPEA exhibits a single FCC structure over a wide temperature range, i.e., from 767 to 1392 °C, which is consistent with the XRD results. It suggests that the chosen heat treatment temperatures (ranging from 900 to 1200 °C) are within the single FCC phase range. The other phases mentioned in the calculated phase diagram are unlikely to form during the process due to insufficient nucleation conditions induced by the water quenching process.

3.2. Microstructure

To ascertain the phase constitution and microstructure, BSE images

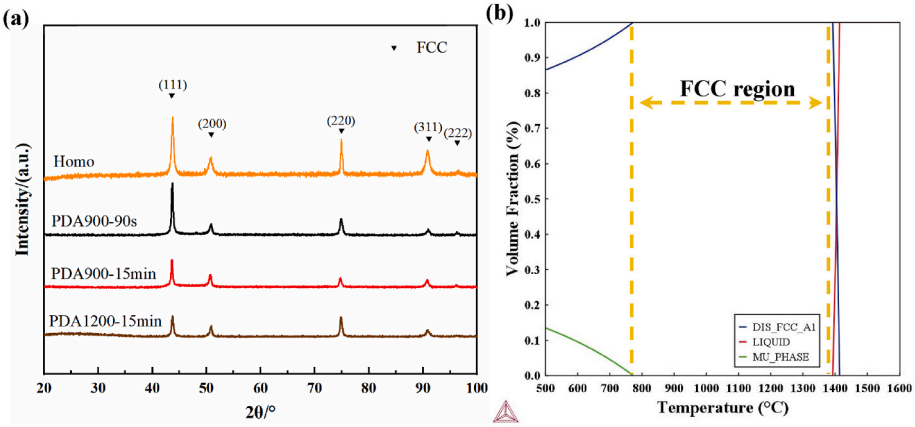

Fig. 1. (a) XRD patterns of the selected samples; (b) Calculated phase diagram of the studied alloy.

of the selected samples are shown in Fig. 2, while the others are provided in Fig. S1. The Homo sample (Fig. 2(a)) exhibits a large grain size without any precipitates in the grains or grain boundaries. After undergoing cold rolling and annealing treatment, the samples exhibit typically equiaxed grains (Fig. 2(b)–(e)), revealing a recrystallized microstructure with no observable precipitates. Notably, there is a prominent gradual increase in grain size with increasing annealing temperature. Fig. 2(f) stitched together from several BSE images

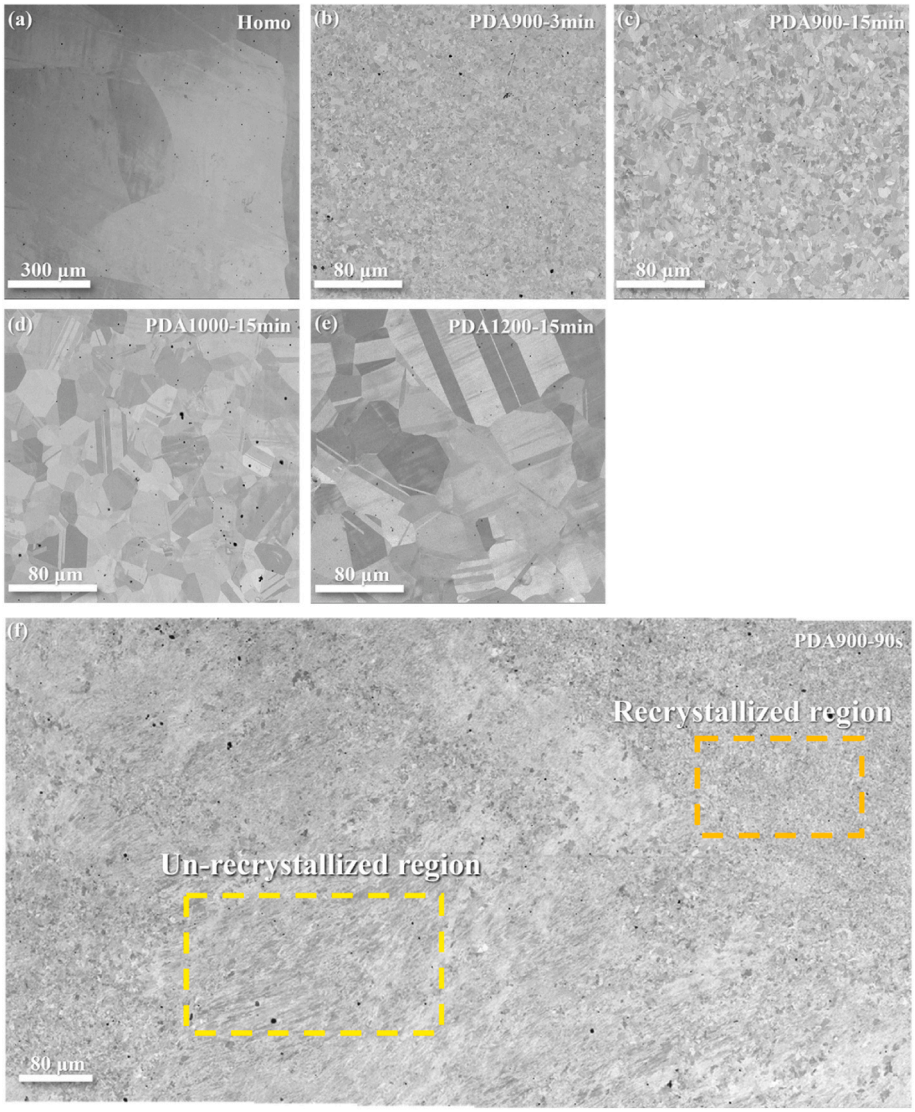

Fig. 2. BSE images of the samples after different treatments. (a) Homo; (b) PDA900-3min; (c) PDA900-15min; (d) PDA1000-15min; (e) PDA1200-15min; (f) PDA900-90s.

illustrates the microstructure of PDA900-90s sample, revealing a heterogeneous structure attributed to the inhomogeneity of the recrystallization process. This sample contains fully recrystallized region (marked by the orange rectangular) and un-recrystallized region (marked by the yellow rectangular), and their volume fractions are estimated to be ~47.1 vol% and ~52.9 vol%, respectively.

TEM images of PDA900-90s and PDA900-15min samples are shown in Fig. 3. The PDA900-90s sample consists of un-recrystallized regions and recrystallized regions with annealing twins (Fig. 3(a_2)), while the SAED pattern (Fig. 3(a_1)) along [011] zone axis confirms the disordered FCC structure of the MPEA. Additionally, high-magnification BF-TEM image and HRTEM images with corresponding FFT patterns in Fig. 3(b)–(d) indicate the presence of defects, i.e., high-density dislocations, twins, and stacking faults (marked by the white rectangular) in the un-recrystallized region. The BF-TEM image and SAED patterns of PDA900-15min are shown in Fig. 3(e), confirming the presence of the same disordered FCC structure and annealing twins. In Fig. 3(f), the HRTEM images and FFT patterns demonstrate that no evident defects exist in the fully recrystallized grain.

The compositional analysis of PDA900-15min sample using the EDS/TEM (Fig. 4) indicates that no evident elemental segregation is observed, confirming this sample has a single FCC structured solid-solution phase. The nominal and experimental compositions of the MEPA are listed in Table 1, suggesting that they have almost identical compositions.

EBSD results of the PDA900-90s are depicted in Fig. 5. The inverse pole figure (IPF) map indicates the coexistence of recrystallized region and un-recrystallized region. Clearly, the recrystallized region is composed of equiaxed grains with abundant annealing twins. Additionally, the kernel average misorientation (KAM) map reveals higher misorientation in the un-recrystallized region, suggesting the accumulation of high-density geometrically necessary dislocations (GNDs) in this area. The grain orientation spread (GOS) map reveals that the volume fractions of the recrystallized region and un-recrystallized region are ~79 vol% and ~21 vol%, respectively. Note that the EBSD images are quite limited, and accordingly the estimated volume fractions are not reliable. Thus, the volume fractions of the recrystallized region and un-recrystallized region were taken from the BSE images.

Microstructural evolution of the fully recrystallized samples is depicted in Fig. 6. As observed in the orientation map, the average grain size of the MPEA gradually increased from ~1.4 to ~47.8 μm with the increasing of annealing time and temperatures. IPF maps of other recrystallized samples are shown in Fig. S2, and the grain size distribution map concluded from the EBSD results is exhibited in Fig. S3. In the meantime, specific values of grain sizes for different samples are listed in Table 2. In addition to the variation in average grain size, the standard deviation of grain size follows a similar trend, which is consistent with observations reported in FCC alloys subjected to the similar process [33,34].

3.3. Mechanical properties

Fig. 7 displays the tensile properties of the alloys at 298 K and 77 K, with the yield strength (σ_y), ultimate tensile strength (σ_{uts}), and total elongation (ε_{te}) are listed in Table 2. At 298 K, the PDA900-90s sample possesses the highest strength, with a σ_y of ~1083 MPa, a σ_{uts} of ~1247 MPa, and a ε_{te} of ~24.2 %, respectively. Meanwhile, for the recrystallized samples, the strength decreases (σ_y: from ~811 MPa to ~359 MPa, σ_{uts}: from ~1131 MPa to ~836 MPa) with longer annealing time and higher annealing temperatures, while the ductility exhibits the opposite trend, i.e., ε_{te} is increased from ~40.2 % to ~64.3 %. Additionally, the engineering tensile stress-strain curves of the other recrystallized samples are shown in Fig. S4. There is an evident relation between the mechanical strength and average grain sizes, which will be discussed hereinafter. Overall, the mechanical strength of this MPEA has been significantly enhanced by cold rolling and PDA annealing treatments compared to the Homo sample (σ_y: ~252 MPa, σ_{uts}: ~546 MPa, ε_{te}: ~60.3 %).

It is worth noting that there is a yield platform in the engineering

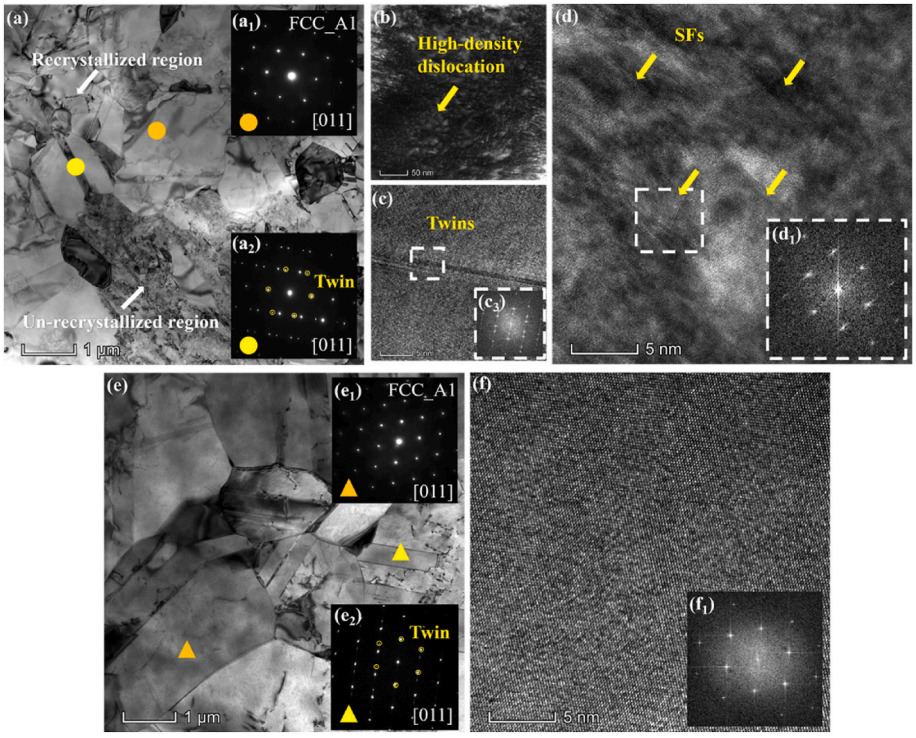

Fig. 3. (a) BF-TEM image of PDA900-90s with SAED patterns taken along [011] corresponding to the recrystallized region; (b–d) HR-TEM images of the un-recrystallized region and corresponding FFT patterns of the selected region; (e) BF-TEM image of PDA900-15min with SAED patterns taken along [011]; (f) HR-TEM of PDA900-15min and corresponding FFT pattern.

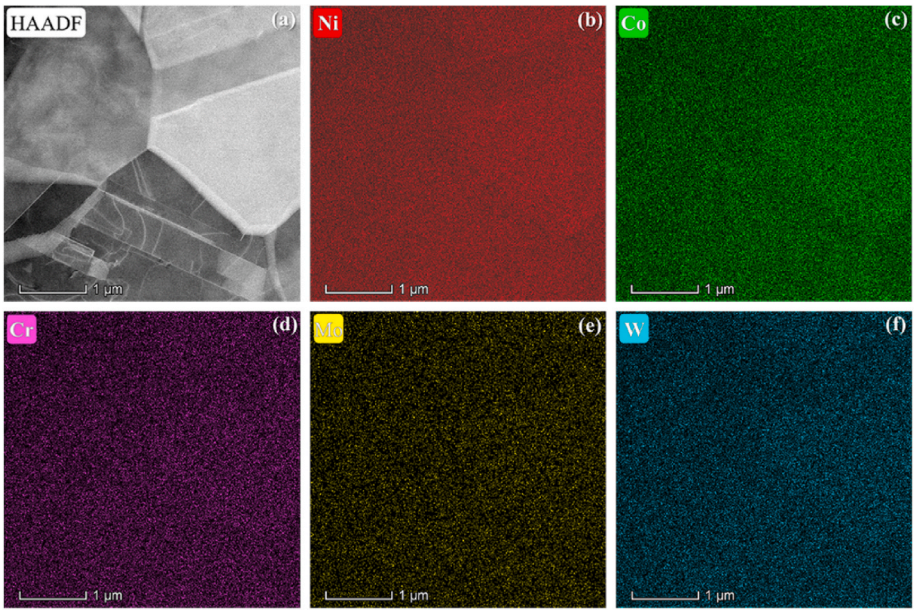

Fig. 4. (a) HAADF image of PDA900-15min and (b–f) EDS element mapping of the MPEA with the element of Ni, Co, Cr, Mo, W.

Table 1
Nominal and experimental compositions of this alloy (in at. %).

	Ni	Co	Cr	Mo	W
Nominal	48	33	9	4	6
Experimental	48.4 ± 0.32	33.50 ± 0.48	8.61 ± 0.27	4.13 ± 0.21	5.33 ± 0.57

tensile stress-strain curves of the PDA900-15min sample, inducing an up-turn in the corresponding work-hardening rate curve. This phenomenon was also observed in deformation-twin-strengthened CoCrNi medium-entropy alloy [35] and precipitate-strengthened superalloys [36], which have been shown to maintain a higher work-hardening rate and improved ductility [37,38]. As for the other samples, the work-hardening rate curves present similar tendency, which steeply drops within the elastoplastic transition stage, and then slowly decreases as the plastic deformation further increases, and finally deteriorates drastically to fracture.

At 77 K, the selected samples show enhanced mechanical properties with synergetic improvement of strength and ductility. In addition to significant increases in ductility, the values of σ_y are also enhanced noticeably, i.e., from ~1083 MPa to ~1407 MPa for PDA900-90s, from ~811 MPa to ~1085 MPa for PDA900-3min, from ~682 MPa to ~880 MPa for PDA900-15min, from ~420 MPa to ~692 MPa for PDA1000-15min, from ~359 MPa to ~573 MPa for PDA1200-15min. Note that the enhancement of PDA1000-15min and PDA1200-15min samples

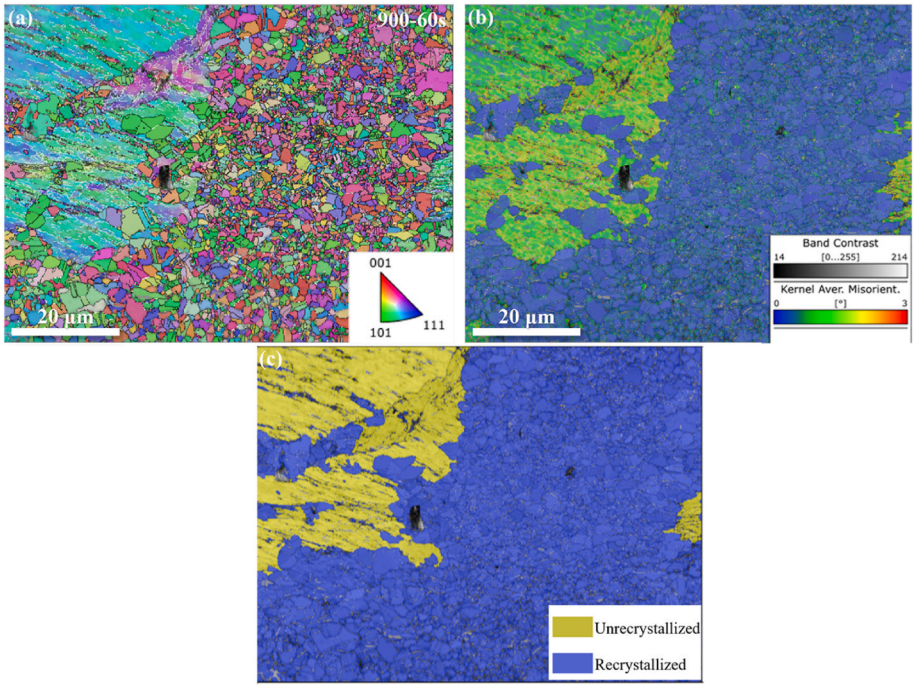

Fig. 5. EBSD analysis of PDA900-90s with recrystallized and un-recrystallized region: (a) IPF map; (b) KAM map; (c) GOS map.

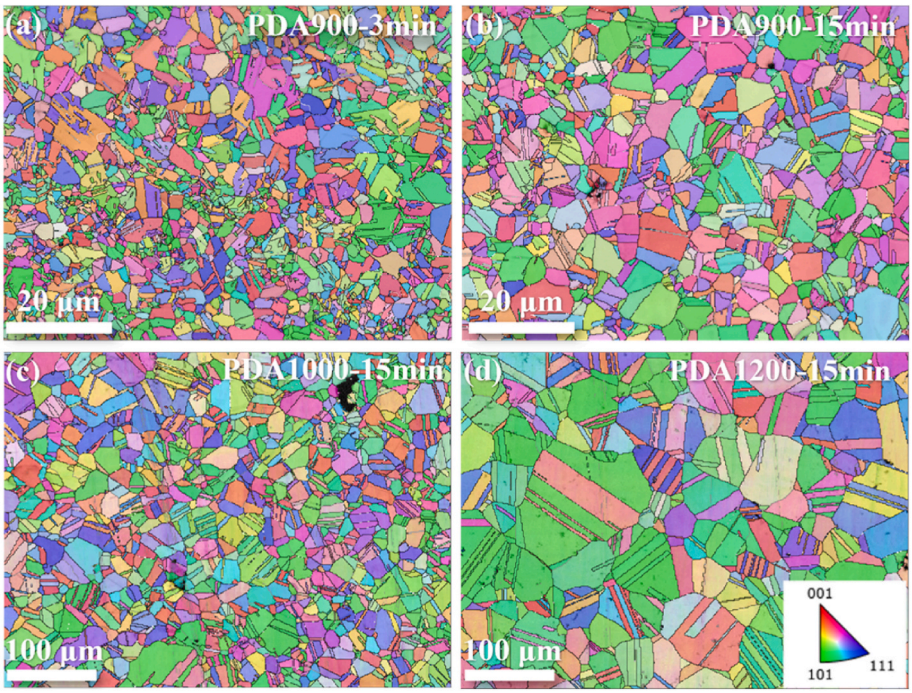

Fig. 6. IPF maps of the samples: (a) PDA900-3min; (b) PDA900-15min; (c) PDA1000-15min; (d) PDA1200-15min.

Table 2
Average grain size and mechanical properties of the samples at 298 K and 77 K.

Samples	Temperature (K)	Yield Strength (MPa)	Ultimate Tensile Strength (MPa)	Total Elongation (%)	Average Grain Size (μm)
PDA900-90s	298	1083	1247	24.2	1.4
	77	1407	1699	30.6	
PDA900-3min	298	811	1131	40.2	1.4
	77	1085	1620	42.7	
PDA900-15min	298	682	1063	50.4	2.9
	77	880	1535	62.3	
PDA1000-15min	298	420	929	60.6	19.0
	77	692	1405	68.7	
PDA1200-15min	298	359	859	65.5	34.9
	77	573	1270	80.8	
Homo	298	252	546	60.3	–
	77	413	848	71.3	–

exceeds 50 %. The corresponding work-hardening rate curves shown in Fig. 7(d), suggests that the work-hardening rate could be significantly improved at lower temperature, ascribing to the existence of deformation twins.

4. Discussion

4.1. Strengthening mechanisms

At ambient temperature, the current MPEA achieved the synergetic improvement of strength and ductility through appropriate treatment. The selected PDA900-90s, PDA900-3min and PDA900-15min samples possess excellent strength compared with the reported single FCC structure MPEAs at 298K, as shown in Fig. 8(a). Compare to the equi-atomic CoCrNi base alloy with the mean grain size of ~1.26 μm [39], the PDA900-3min (mean grain size: ~1.4 μm) sample showed remarkable improvement in yield strength (from ~420 MPa to ~811 MPa), maintaining a good ductility of ~40.2 %. In addition, for most single-phase alloys, the optimum grain size served as a valid indicator to analyze the strength-ductility combination [16], which indexed by: $\varepsilon_{te} \times (\sigma_y + \sigma_{uts})/2$. During the process of plastic deformation, the GNDs accumulated at grain boundary and interior, introducing plastic strain gradient in these regions, which contributes to achieving extreme effects of grain-boundary strengthening. Thus, the optimum grain size could be considered as the critical value to achieve the strength-ductility combination through grain-boundary strengthening. Relevant data is plotted in Fig. 9(a), the optimum grain size of this MPEA is ~2.9 μm (PDA900-15min).

As for the studied MPEA with homogenous equiaxed grains, the yield strength consists of intrinsic lattice resistance to dis-location motion (σ_i), solid-solution strengthening (σ_{ss}), and grain-boundary strengthening (σ_{gb}), expressed as follows:

$$\sigma_y = \sigma_i + \sigma_{ss} + \sigma_{gb} \tag{1}$$

To further reveal the strengthening mechanism of this MPEA, the Hall-Petch equation was concluded from Table 2:

$$\sigma_y = \sigma_o + k_{HP} \bullet d^{-1/2} \tag{2}$$

where σ_o is the sum of σ_i and σ_{ss} (indicating the lattice friction stress in MPEAs), k_{HP} is the Hall-Petch coefficient (MPa/μm$^{1/2}$), and d is the average grain size (μm). In Fig. 9(b)–a linear relationship is observed, and the slope and intercept are calculated to be ~261 MPa and ~676 MPa/μm$^{1/2}$, respectively. Thus, the sum of σ_i and σ_{ss} is ~261 MPa, and the k_{HP} is ~676 MPa/μm$^{1/2}$. Additionally, the dependence of yield strength on the grain size of this alloy is satisfactory among the other alloys, as shown in Fig. 9(c).

The lattice distortion induced by atomic volume misfit effectively hindered the dislocation motion, contributing to the higher solid-solution strength. According to the previous study [13], the contribution of the volume misfit to strengthening can be estimated by δ parameter [40–44]:

$$\delta = \frac{\sqrt{\sum_n c_n \Delta V_n^2}}{3V_{alloy}} \tag{3}$$

where c_n refers to the concentration of composition, $\Delta V_n = V_n - V_{alloy}$ is the misfit volume of each type-n constituent element, V_n is the apparent

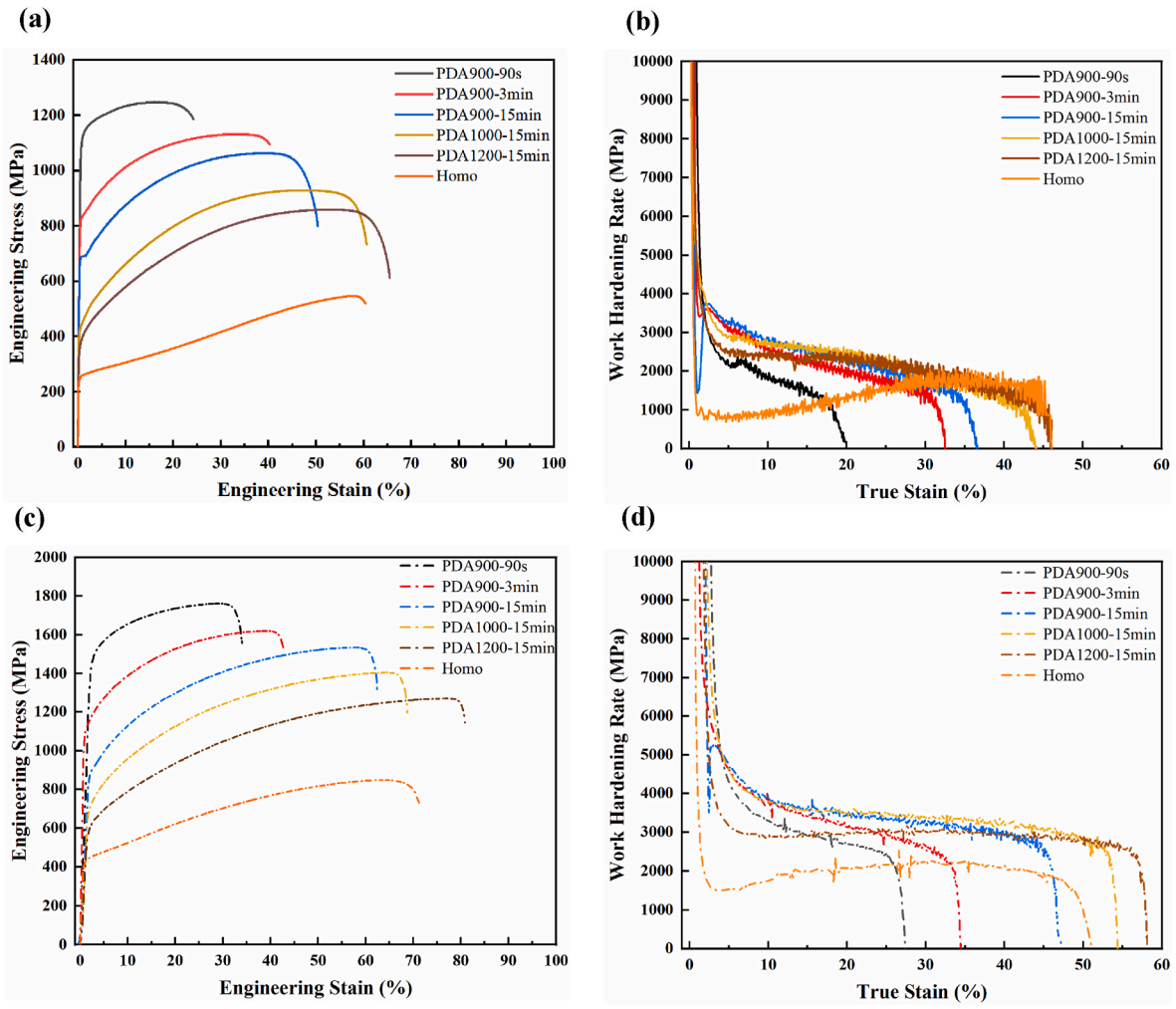

Fig. 7. Engineering tensile stress-strain curves of the selected samples: (a) at 298 K; (c) at 77 K. And the work-hardening rate curves (b) at 298 K; (d) at 77 K.

volume of elements in FCC-structured alloy, $V_{alloy} = \sum_n c_n \cdot V_n$ is the alloy atomic volume, and the required apparent volume of elements (V_n) are as follows: Ni ~10.94, Co ~11.12, Cr ~12.27, Mo ~16.04, W ~16.46 (Å^3) [13,45]. Compared with the reported FCC structured alloy, i.e., $Ni_{63.2}V_{36.8}$ ~3.834, NiCo ~0.272, NiCoV ~3.647, NiCoCr ~1.716, CoCrFeNi ~1.672, CoCrFeMnNi ~1.850 [42], this MPEA presents severe volume misfit of ~4.458, ascribing to the addition of Mo and W elements. Hence, the method developed by Labusch could be used to calculate the value of solid-solution strengthening [46–48]:

$$\Delta\sigma_s = M \bullet \frac{G \bullet \varepsilon_s^{2/3} \bullet c^{1/2}}{700} \tag{4}$$

$$G = \frac{E}{2(1+\mu)} \tag{5}$$

Wherein M is the Taylor factor (constant for FCC-structure alloy: 3.06), G is the shear modulus obtained from Poisson's ratio ν (0.3 for NiCoCr system [49]) and shear modulus $\underline{E}$ (212 GPa for this alloy), c refers to the concentration of the solute in this alloy (Cr, Mo, W elements), ε_s is the parameter to access the size and modulus misfit around the solute atoms, as follows:

$$\varepsilon_s = \sqrt{\varepsilon_G^2 + \alpha^2 \varepsilon_a^2} \tag{6}$$

$$\varepsilon_G = \frac{1}{G} \bullet \frac{\partial G}{\partial c};\ \varepsilon_a = \frac{1}{a} \bullet \frac{\partial a}{\partial c} \tag{7}$$

where α serves as a dimensionless parameter that accounts for the difference in the interaction forces between the screw ($\alpha = 3$) and edge ($\alpha = 16$) dislocations [50]. Furthermore, ε_a and ε_G, the change of lattice constant and modulus induced by the addition of solute atoms, could be assumed by the linear relationship between NiCo (3.534, 84) [49] and this alloy (3.592, 84) since the σ_{ss} of this alloy is 64 MPa (screw dislocation dominate) and 197 MPa (edge dislocation dominate). The solid solution strength of the MPEA located in this interval, attributing to the coexistence of screw and edge dislocations. The proportion of dislocation type cannot be accurately measured, thus the strength contribution induced by volume misfit integrates into the lattice friction stress (σ_o). Furthermore, the relationship between the atomic radius differences of the alloy and the dominant dislocation type was proposed by Li et, al [13]. The difference in atomic volume breaks the spherical symmetry of the stress field introduced by solute atoms addition, allowing screw dislocations to play a leading role in strengthening during the deformation process. This theory explained the correlation between the severe volume misfit induced by solutes and the deviation of σ_{ss} to a certain extent. Additionally, it has been reported that Mo/W addition introduced brittle intermetallic compounds at grain boundaries which devastate the ductility [31,51]. Whereas in this work, Mo and W elements dissolved into the matrix through component regulation and proper homogenization treatment. Thus, this alloy finally achieved effective solid-solution strengthening.

Differing from the samples with equiaxed grains, the hetero-structured sample displays higher strength owing to the HDI strength-

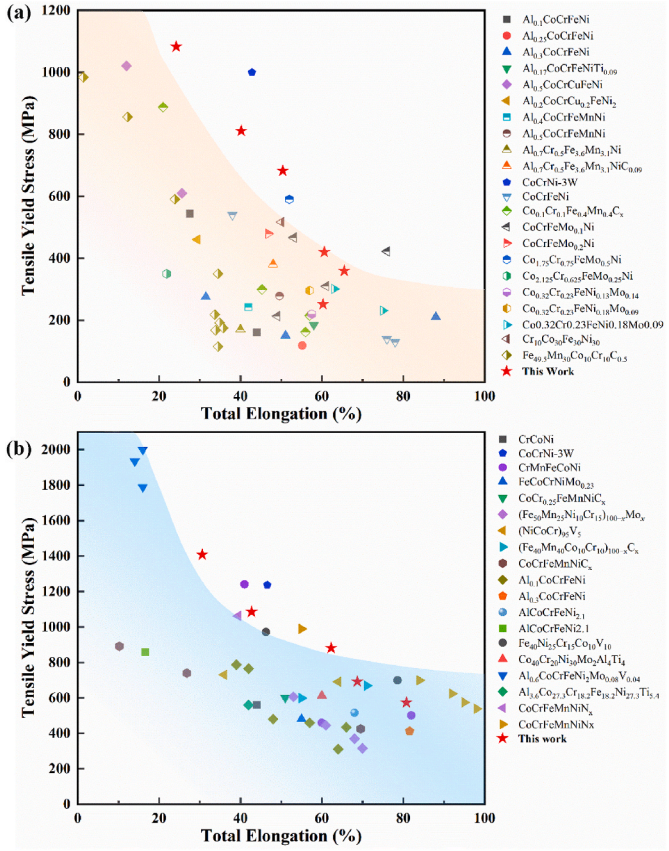

Fig. 8. Comparison of the engineering yield strength and total elongation between the studied MPEA after different treatments and (a) the reported single-FCC structured MPEAs at 298 K; (b) some typical MPEAs at 77 K (references are listed in Tables S1–S2).

ening induced by the inhomogeneous plastic deformation [52,53]. To further evaluate the strengthening mechanism of the hetero-structured sample, the loading-unloading-reloading (LUR) cyclic tensile test was conducted to analyze the back stress (σ_b) quantitatively [54]. Fig. 10(a) shows the LUR curve of PDA900-90s sample, and the hysteresis loop in the second load displayed in Fig. 10(b) illustrates the calculation method as follows:

$$\sigma_b = \frac{\sigma_u + \sigma_r}{2} \tag{8}$$

$$\sigma_{eff} = \sigma_{flow} \quad \sigma_b \tag{9}$$

where σ_{flow} is the flow stress, σ_{eff} is the non-directional short-range local stress required for a dislocation to move, and σ_b refers to the directional long-range internal stress caused by the pile-up of GNDs [55], σ_{up} is reloading yield stress, σ_{down} is unloading yield stress. The evolution of σ_b, σ_{eff}, and σ_{flow} are plotted in Fig. 10(c), the σ_b and σ_{eff} increased simultaneously accompanied by increasing true strain, except for the sixth load. The proportion of the back stress is over 50 %, indicating the dominant role of the back stress in the strengthening mechanism. For this hetero-structured alloy, the HDI strengthening is another constituent of engineering yield strength compared with the homo-structured alloy, expressed as follows:

$$\sigma_y = \sigma_i + \sigma_{ss} + \sigma_{gb} + \sigma_{HDI} \tag{10}$$

wherein the sum of σ_i and σ_{ss} is 261 MPa, σ_b is calculated based on the first hysteresis loop near the yield point (~629 MPa), and σ_{gb} (~267 MPa) is taken from the aforementioned Hall-Petch equation (grain size: ~1.4 μm) with the volume fraction of the recrystallized region (~47.1 %). It is to be further analyzed that the predicted yield strength (~1157 MPa) slightly deviates from the experimental value (~1084 MPa), which could be primarily interpreted as a statistical error of the phase fraction and the grain size of the recrystallized region.

The contribution of the yield strength can be divided into two parts, which are classified based on their temperature dependence. The temperature-independent part relates to the obstacles hindering the dislocation within a long range (>10 nm), indicating the grain/annealing twin boundary of this MPEA. Additionally, the temperature-dependent part is considered as the lattice friction stress (σ_0), reflecting the resistance of dislocation thermal activation within a short range (<10 nm), and the lattice friction stress is a manifestation of the solid solution strengthening effect. Hence, the cryogenic environment will have a significant impact on the solute-strengthening contribution of this MPEA [25,49,56,57].

To reveal the variation of the strengthening mechanism at 77 K, the Hall-Petch relation is concluded, plotted in Fig. 9(d). Wherein σ_0 is 488 MPa, and the Hall-Petch coefficient is 698 MPa/um$^{1/2}$. Compared with the ambient temperature (298 K), the lattice friction stress increased due to higher thermal-activated energy at lower temperature, while a slight increase of the Hall-Petch coefficient is observed.

As for the heterogeneous structure, the un-recrystallized region is considered as the long-range obstacle, serving as a thermal-independent part. Hence the effect of cryogenic temperature on the back stress will be slight. To elucidate this conclusion, the HDI stress should be departed from the yield strength at 77 K. Referring to Eq (5), the back stress could be given as:

$$\sigma_{HDI} = \sigma_y \quad \sigma_i \quad \sigma_{ss} \quad \sigma_{gb} \tag{11}$$

Where the sum of σ_i and σ_{ss} is lattice friction stress σ_0 (488 MPa), and σ_{gb} is 279 MPa using the prediction method mentioned above. Thus, the HDI stress (77 K) is ~640 MPa, slightly higher than that of at 298 K (~629 MPa), confirming that the HDI stress strengthening is thermal-independent.

4.2. *Deformation mechanisms*

Due to the Mo and W co-doping, the SFE of this alloy significantly decreased and facilitated the formation of annealing twins, SFs and DTs. Besides, the severe lattice distortion induced by the Mo and W addition promote the generation of screw dislocation and the cross-slip. The divergent deformation mechanisms mentioned above are conductive to maintaining higher work hardening rate. Thus, a detailed study was carried out to reveal the deformation mechanism at ambient and cryogenic temperature.

The deformation microstructure of PDA900-90s and PDA900-15min samples within different strains at 298K are displayed in Figs. 11 and 12, respectively. Regarding the PDA900-15min with equiaxed grains (in Fig. 11(a)–(d)), slip traces are observed in some grains at a strain of ~1.5 %. With a higher strain of ~10 %, the increasing internal stress can activate cross-slip, indicating that the dislocations predominate plastic deformation at early stage. Moreover, more details could be revealed by TEM image after fracture. The interaction between the annealing twin boundary and the high-density dislocation shown in Fig. 11(e)–(f) manifests that the annealing twins can be considered as an obstacle to restrict the dislocation. While high-density dislocation piled up could stimulate the twin boundary to become a Frank-Read source [58], which is prone to maintaining work-hardening rates by propagating more dislocations. Apart from the dislocation cells, SFs and Lomer-Cottrell locks (L-C locks) are also identified in the same area, reducing the mean free path of dislocations slip, according to the HRTEM image and SAED pattern in Fig. 11(g)–(h). It could conclude that dislocations and SFs play a dominant role in the deformation process.

Regarding PDA900-90s, this sample possesses higher strength due to the existing deformation structure in un-recrystallized region. In Fig. 12

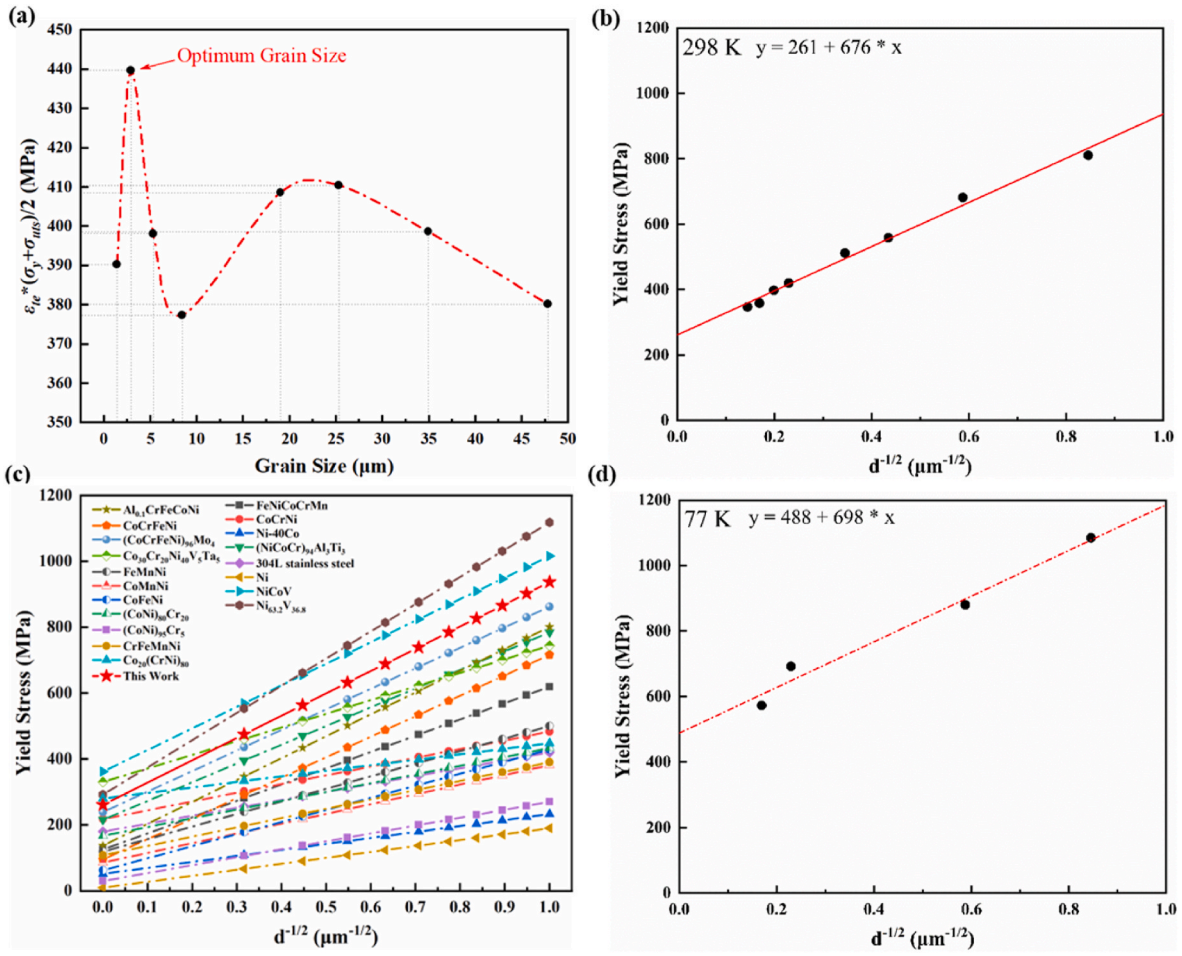

Fig. 9. (a) The plot of optimum grain size indexed by $\varepsilon_{te} \times (\sigma_y + \sigma_{uts})/2$; (b) the Hall-Petch relation of this alloy at 298 K; (c) Dependence of yield strength on the grain size of this alloy and some MPEAs (references are listed in Table S3); (d) the Hall-Petch relation of this MPEA at 77 K.

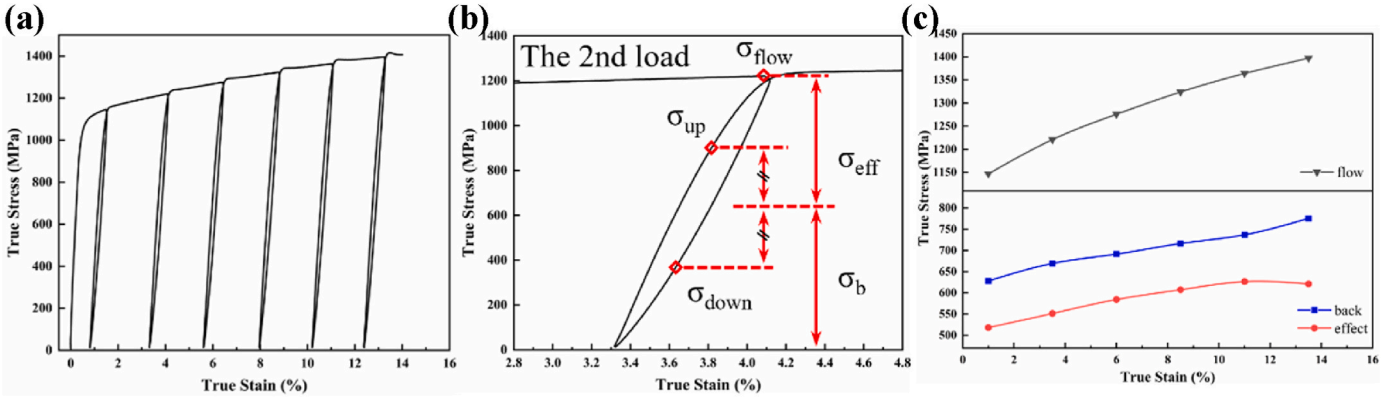

Fig. 10. (a) LUR true stress-strain curve of PDA900-90s; (b) magnification of the second hysteresis loop; (c) true stress evolution of σ_{flow}, σ_b, and σ_{eff} with increasing true strain.

(a)–(d), nano-sized deformation twins and discrete dislocations are detected in the equiaxed grain near the un-recrystallized region at the strain of ~1.5 %. More deformation twins and higher density dislocations are observed as the strain increased to ~10 %, indicating that enough stress has been applied to induce deformation twins. To further expound this phenomenon, the critical stress required for twinning is shown as follows [59]:

$$\sigma_T = \frac{2\gamma_{SFE}}{m \bullet b_p} \tag{12}$$

Where σ_T is the critical stress, γ_{SFE} is the stacking fault energy (taken from the NiCoCr [60], 26 mJ/m ^{2}), m is the Schmid factor (0.33 for most alloys [59]), and b_p is the Burgers vector of the Shockley partial dislocation (1/6a [112] for FCC, 0.1466 nm). The estimated σ_T is about ~1074 MPa at 298 K, and the yield strength of PDA900-90s is ~1083

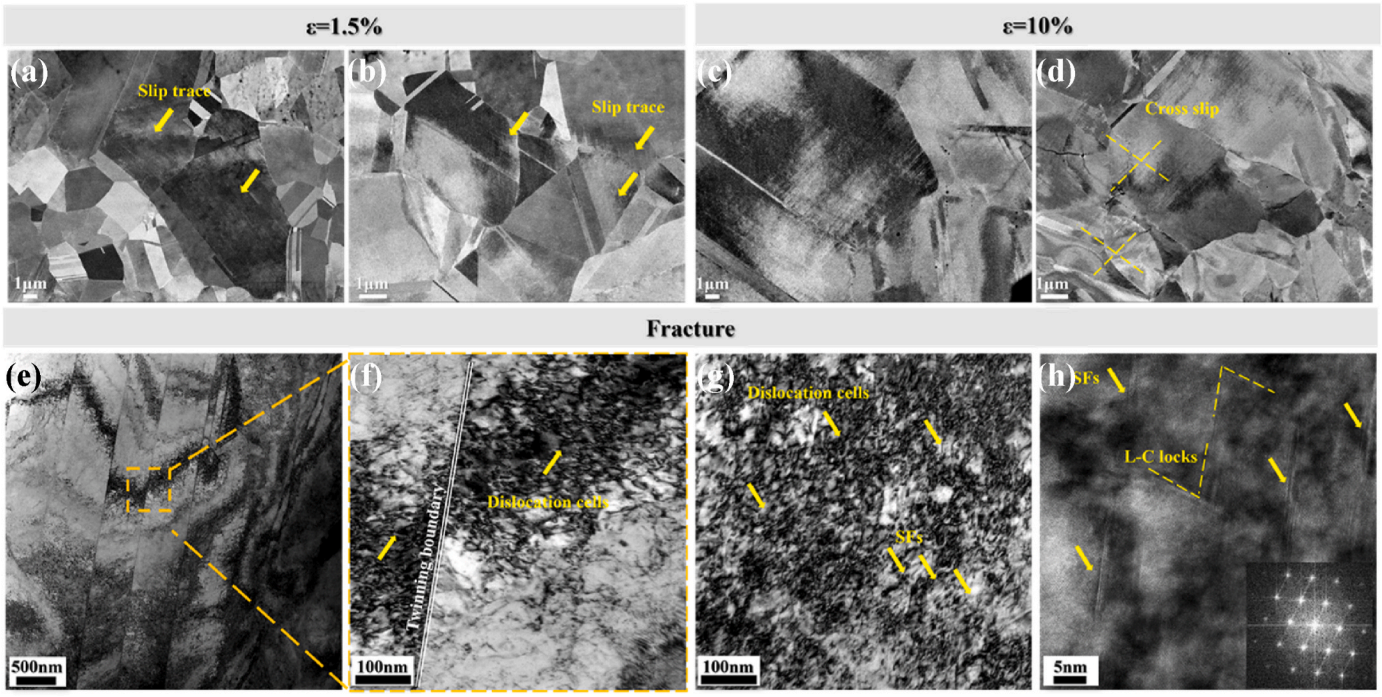

Fig. 11. The deformation microstructure of PDA900-15min at 298 K. ECCI images at the tensile strain of (a–b) ~1.5 %, (c–d) ~10 %. (e–f) BF-TEM images of the fractured sample; (h) HR-TEM image and corresponding FFT pattern of L-C locks.

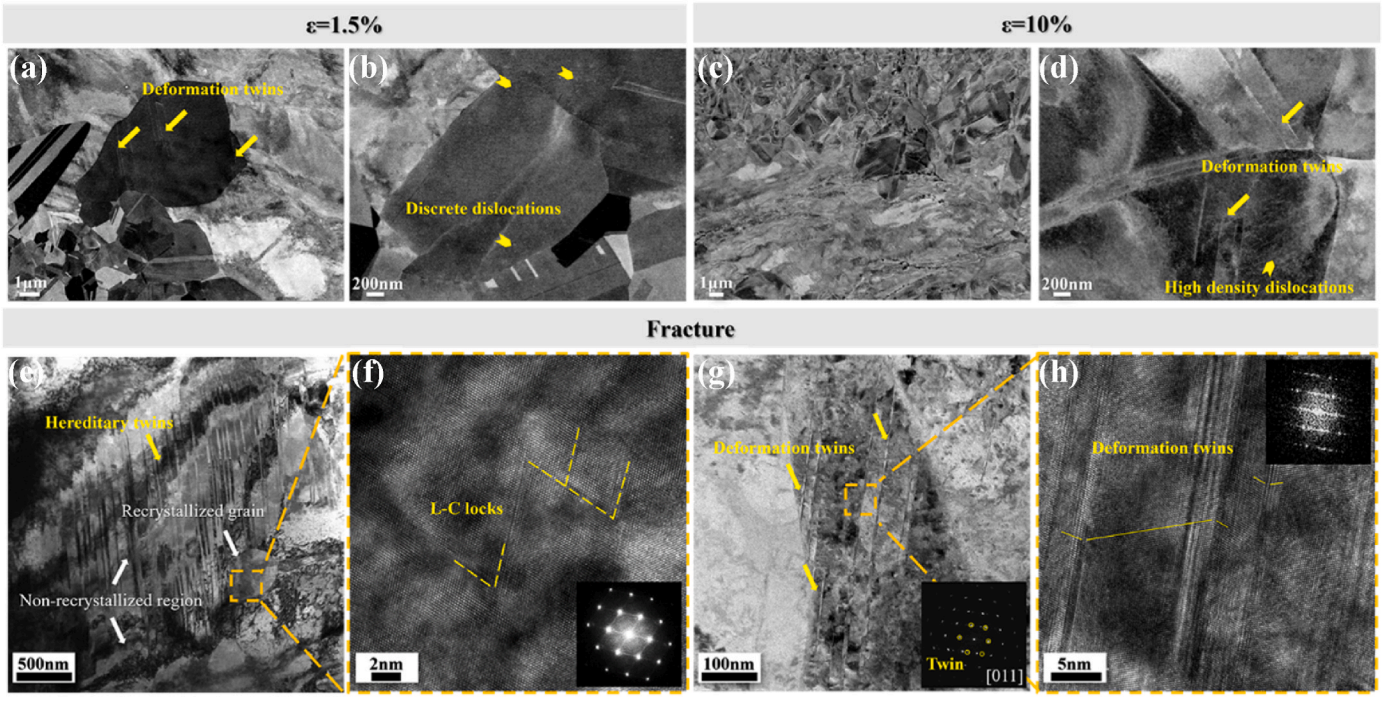

Fig. 12. The deformation microstructure of PDA 900-90s at 298 K. ECCI images at the tensile strain of (a–b) ~1.5 %, (c–d) ~10 %, (e) BF-TEM images of the fractured sample, (f) HR-TEM image and corresponding FFT pattern of L-C locks, (g) BF-TEM images of the fractured sample and the SAED pattern of DTs, (h) HR-TEM image and corresponding FFT pattern of DTs.

MPa, validating the appearance of deformation twins. As the deformation further proceeds to fracture, high-density deformation twins and dislocation cells could be identified in Fig. 12(e)–(f). Meanwhile, the L-C locks (with faint streaks in the SAED pattern) in the recrystallized grain and the hereditary deformation twins in the un-recrystallized region are shown in Fig. 12(g)–(h). In a word, the conjugated effect of high-density dislocation, L-C locks, and deformation-induced twinning are applied to achieve synergetic improvement of strength and ductility [61–63].

The effect of HDI strengthening depends on the structure. For most eutectic and multi-phase alloys, the significant difference between the phases leads to a large accumulation of GNDs at the incoherent interface, which significantly affects the HDI strengthening [64,65].

However, at non-cohesive interfaces, it is also prone site for crack initiation and subsequently damages the plasticity of alloys. When it comes to the heterogeneous structures with coherent interface, the varying grain sizes and partial recrystallization, GNDs also accumulate at the interface. These structures present pronounced HDI strengthening effect, whilst the probability of crack generation is significantly reduced and conduce to maintain ductility. Furthermore, the non-coordinated deformation between the recrystallized region and the unrecrystallized region was revealed by quasi-in-situ EBSD shown in Fig. 13. With the gradual increase in deformation, GNDs piled up in the grain boundary which located in the interface between the recrystallized region and the unrecrystallized region (marked by red arrows), confirming the HDI stress strengthening induced by the non-coordinated deformation. In addition, the recrystallized grains surrounded by the unrecrystallized region presented obvious delayed deformation compared to the recrystallized region (marked by white arrows), less GNDs accumulated in these grains. And the non-simultaneous deformation confirmed that the unrecrystallized region delivered the stress to the recrystallized grains during the deformation and went through plastic deformation within high enough stress.

Combining with work-hardening rate curves in Fig. 7, the non-coordinated deformation within the heterogeneous structure presents obvious work-hardening effects at the initial stage, contributing to the higher strength. In comparison to the recrystallized sample with homogeneous structure, the heterogeneous structure sample possesses an un-recrystallized region maintained high-density dislocation from the cold-rolling process, providing less region to store GNDs during deformation. Hence, at the later stage, it is difficult to relieve the stress concentration, which induces the final fracture.

The fractured morphologies of PDA900-15min and PDA900-90s sample at 77 K are shown in Fig. 14. Nano-sized deformation twins and high-density dislocations coexist in the fractured PDA900-15min sample, while deformation twins dominated in the fractured PDA900-90s sample, possessing higher density due to the higher flow stress. At ambient temperature, dislocations, SFs and L-C locks apply critical role in deformation, only a few deformation twins existed in the fractured PDA900-90s sample. While the cryogenic environment is beneficial for the activation of deformation twins, the observation of high-density deformation twins is attributed to the lower temperature-dependent γ_{SFE}. As mentioned in Eq (12), lower critical stress is required for twinning. The alloys achieved higher work-hardening rates at 77 K compared to 298 K (in Fig. 7), attributing to the high-density deformation twins. And the high work-hardening rate is considered the primary reason for preventing necking, which helps to achieve high strength and ductility. Furthermore, the intersection between the deformation twins can further hinder the dislocation operation, which is so-called dynamic Hall-Petch effect, so that the work-hardening rate paradoxically increases to reach the synergistical improvement of strength and ductility [27].

5. Conclusions

In this work, a single-phase FCC structured $Ni_{48}Co_{33}Cr_9Mo_4W_6$ MPEA was designed and fabricated. A comprehensive array of tests and characterizations were employed to investigate microstructural evolution, mechanical behavior, strengthening and deformation mechanisms. The key conclusions can be drawn as follows:

(1) The cold rolled $Ni_{48}Co_{33}Cr_9Mo_4W_6$ MPEA with a single FCC phase was processed by different PDA annealing treatments. The average grain sizes ranging from ~1.4 μm to ~47.8 μm were achieved in the samples with homogenous grains and single FCC structure. Undoubtedly, the PDA900-3min sample with the smallest grain size (~1.4 μm) possessed the best combination of strength and ductility among all the homogenous samples. In detail, it exhibited a yield strength of ~811 MPa, an ultimate tensile strength of ~1131 MPa, and a total elongation of ~40.2 % at ambient temperature (298 K). At LN_2 temperature (77 K), all the homogenous samples showed higher strength and better ductility.

(2) Utilizing a short time annealing at 900 °C, a heterogeneous microstructure composed of fully recrystallized (~47.1 vol%) and partial un-recrystallized (~52.9 vol%) regions was realized in the PDA900-90s sample. At ambient temperature, its tensile yield strength and total elongation were ~1083 MPa and ~24.2

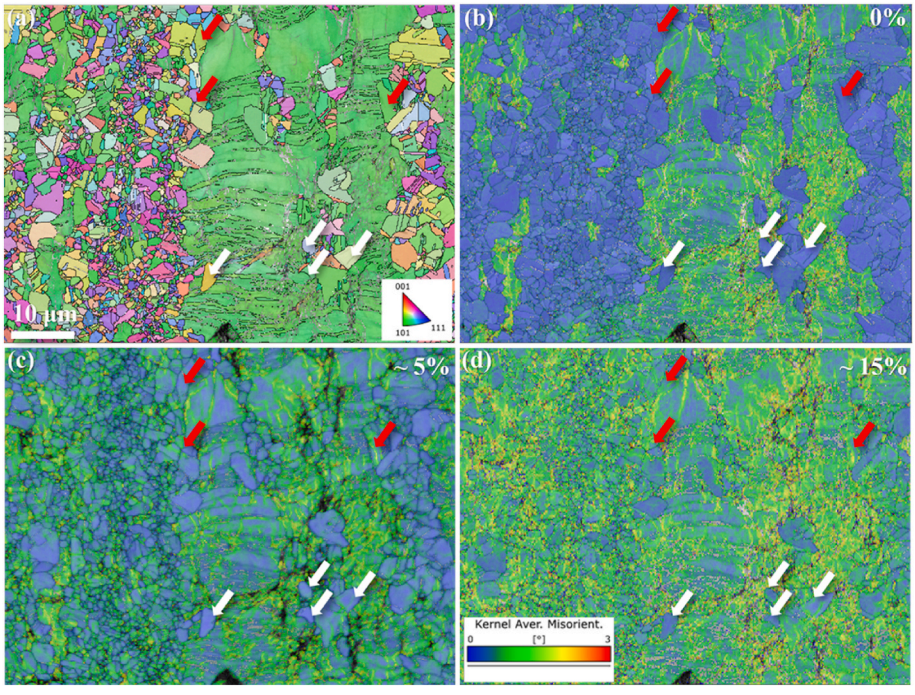

Fig. 13. Quasi in-situ EBSD results of PDA900-90s. (a) IPF map of the selected region, (b–d) KAM maps of the selected region with different strains (~0, 5, 15 %).

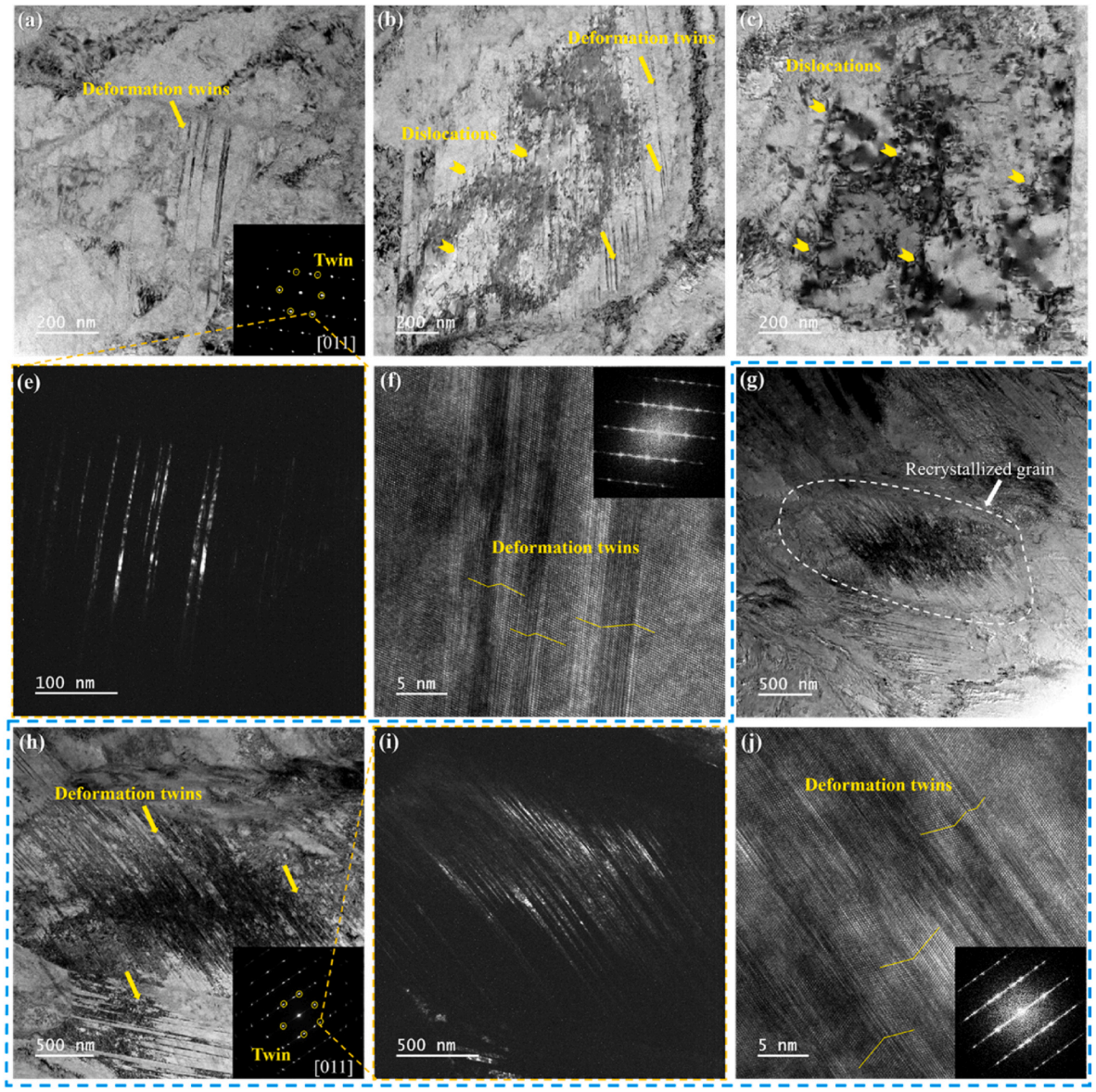

Fig. 14. The deformation microstructure of fractured PDA900-15min and PDA900-90s at 77 K. For PDA900-15min sample, (a–c) BF-TEM image and SAED pattern of deformation twins, (d) DF-TEM image of deformation twins, (e) corresponding HR-TEM image and FFT pattern of deformation twins; For PDA900-90s sample, (f–g) BF-TEM image and SAED pattern of deformation twins, (h) DF-TEM image of deformation twins, (i) corresponding HR-TEM image and FFT pattern of deformation twins.

%, and these values were increased to ~1407 MPa and ~30.6 % at LN_2 temperature (77 K).

(3) Compared to the reported single-phase FCC-structured MPEAs in the literature, both the PDA900-3min and PDA900-90s samples exhibited a more remarkable combination of strength and ductility, indicating that they have successfully achieved an enhanced synergy between strength and ductility. Note that at ambient temperature, the PDA900-3min sample with an average grain size of ~1.4 μm showed noticeably higher yield strength in comparison with the equi-atomic NiCoCr base alloy possessing an average grain size of ~1.26 μm and a yield strength of ~420 MPa. This suggests that Mo and W co-doping is an effective strategy for achieving enhanced strength-ductility synergy in MPEAs with FCC structure.

(4) At 298 K, grain boundary strengthening and solid solution strengthening predominated the homo-structured samples, whereas HDI strengthening occupies the dominant role in the heterogeneous structured sample (PDA900-90s). Additionally, lower temperature (77 K) has significantly influence on the lattice friction stress of the studied $Ni_{48}Co_{33}Cr_9Mo_4W_6$ MPEA, with decreased effects in grain boundary strengthening and HDI strengthening. Deformation mechanisms were also temperature-dependent. At 298 K, dislocations, SFs and L-C locks played vital roles in the deformation of homo- and hetero-structured samples, and only a few DTs were observed in hetero-structured sample during deformation. Conversely, at 77 K, the generation of high-density nano-sized DTs during deformation contributed to the enhancement of strength and ductility. In a word, the coupling of diversified strengthening and deformation mechanisms renders this alloy exceptionally well-suited for cryogenic temperature environments.

CRediT authorship contribution statement

Junchen Liu: Writing – review & editing, Writing – original draft, Investigation, Conceptualization. **Chenliang Chu:** Writing – review &

editing. **Yemao Lu:** Writing – review & editing. **Zhao Tian:** Methodology, Investigation. **Weiping Chen:** Supervision, Funding acquisition, Conceptualization. **Zhiqiang Fu:** Writing – review & editing, Supervision, Funding acquisition.

Declaration of competing interest

The authors declare that they have no known competing financial interests or personal relationships that could have appeared to influence the work reported in this paper.

Data availability

Data will be made available on request.

Acknowledgments

Junchen Liu, Chenliang Chu, Zhao Tian, Weiping Chen and Zhiqiang Fu wish to acknowledge the financial support from the National Natural Science Foundation of China (Grant No. 52103360), the Basic and Applied Basic Research Foundation of Guangdong Province (Grant No. 2023A1515012363), the International Science and Technology Cooperation Project of Guangdong Province (Grant No. 2023A0505050154), the Pearl River Talent Program (Grant No. 2021QN02C766) and the technical support of Sinoma Institute of Materials Research (Guang Zhou) Co., Ltd. Yemao Lu performed this research without funding support.

References

[1] N. Yao, T. Lu, K. Feng, B. Sun, R.Z. Wang, J. Wang, Y. Xie, P. Zhao, B. Han, X. C. Zhang, S.T. Tu, Ultrastrong and ductile additively manufactured precipitation-hardening medium-entropy alloy at ambient and cryogenic temperatures, Acta Mater. 236 (2022) 118142, https://doi.org/10.1016/j.actamat.2022.118142.

[2] Z. Jiang, W. Chen, C. Chu, Z. Fu, J. Ivanisenko, H. Wang, S. Peng, Y. Lu, E. J. Lavernia, H. Hahn, Directly cast fibrous heterostructured FeNi0.9Cr0.5Al0.4 high entropy alloy with low-cost and remarkable tensile properties, Scripta Mater. 230 (2023) 115421, https://doi.org/10.1016/j.scriptamat.2023.115421.

[3] Z. Jiang, W. Chen, Z. Xia, W. Xiong, Z. Fu, Influence of synthesis method on microstructure and mechanical behavior of Co-free AlCrFeNi medium-entropy alloy, Intermetallics 108 (2019) 45–54, https://doi.org/10.1016/j.intermet.2019.02.006.

[4] Y. Lu, X. Gao, L. Jiang, Z. Chen, T. Wang, J. Jie, H. Kang, Y. Zhang, S. Guo, H. Ruan, Y. Zhao, Z. Cao, T. Li, Directly cast bulk eutectic and near-eutectic high entropy alloys with balanced strength and ductility in a wide temperature range, Acta Mater. 124 (2017) 143–150, https://doi.org/10.1016/j.actamat.2016.11.016.

[5] B. Gludovatz, A. Hohenwarter, D. Catoor, E.H. Chang, E.P. George, R.O. Ritchie, A fracture-resistant high-entropy alloy for cryogenic applications, Science 345 (2014) 1153–1158, https://doi.org/10.1126/science.1254581, 1979.

[6] C. Ke, C. Wang, X. Wang, Superior low temperature mechanical properties and microstructure of (NiCoCr)95V5 medium entropy alloy, Intermetallics 162 (2023) 108034, https://doi.org/10.1016/j.intermet.2023.108034.

[7] T. Yang, Y.L. Zhao, Y. Tong, Z.B. Jiao, J. Wei, J.X. Cai, X.D. Han, D. Chen, A. Hu, J. J. Kai, K. Lu, Y. Liu, C.T. Liu, Multicomponent intermetallic nanoparticles and superb mechanical behaviors of complex alloys, Science 362 (2018) 933–937, https://doi.org/10.1126/science.aas8815, 1979.

[8] Y.L. Zhao, T. Yang, J.H. Zhu, D. Chen, Y. Yang, A. Hu, C.T. Liu, J.J. Kai, Development of high-strength Co-free high-entropy alloys hardened by nanosized precipitates, Scripta Mater. 148 (2018) 51–55, https://doi.org/10.1016/j.scriptamat.2018.01.028.

[9] Y.L. Zhao, T. Yang, Y. Tong, J. Wang, J.H. Luan, Z.B. Jiao, D. Chen, Y. Yang, A. Hu, C.T. Liu, J.J. Kai, Heterogeneous precipitation behavior and stacking-fault-mediated deformation in a CoCrNi-based medium-entropy alloy, Acta Mater. 138 (2017) 72–82, https://doi.org/10.1016/j.actamat.2017.07.029.

[10] X. Wang, Y. Ding, H. Yu, Z. Bi, Y. Gao, B. Gan, High strength and ductility in a novel Ni-based superalloy with γ′ and nanotwins/stacking faults architectures, Mater. Sci. Eng., A 847 (2022) 143293, https://doi.org/10.1016/j.msea.2022.143293.

[11] H. Peng, L. Hu, L. Li, W. Zhang, Ripening of L12 nanoparticles and their effects on mechanical properties of Ni28Co28Fe21Cr15Al4Ti4 high-entropy alloys, Mater. Sci. Eng., A 772 (2020) 138803, https://doi.org/10.1016/j.msea.2019.138803.

[12] F. He, S. Wei, J.L. Cann, Z. Wang, J. Wang, C.C. Tasan, Composition-dependent slip planarity in mechanically-stable face centered cubic complex concentrated alloys and its mechanical effects, Acta Mater. 220 (2021) 117314, https://doi.org/10.1016/J.ACTAMAT.2021.117314.

[13] Z. Li, S. Ma, S. Zhao, W. Zhang, F. Peng, Q. Li, T. Yang, C.Y. Wu, D. Wei, Y.C. Chou, P.K. Liaw, Y. Gao, Z. Wu, Achieving superb strength in single-phase FCC alloys via maximizing volume misfit, Mater. Today 63 (2023) 108–119, https://doi.org/10.1016/j.mattod.2023.02.012.

[14] J.-X. Chen, T. Li, Y.-Y. Tan, Y. Chen, H.-Y. Wang, L.-H. Dai, Tailoring nanoprecipitates to achieve ultrahigh strength (CoCrNi)94.5W3Ta2.5 medium-entropy alloys, Mater. Sci. Eng., A 892 (2024) 146046, https://doi.org/10.1016/j.msea.2023.146046.

[15] W. Li, W. Wang, M.C. Niu, K. Yang, J.H. Luan, H.W. Zhang, Z.B. Jiao, Unraveling the two-stage precipitation mechanism in a hierarchical-structured fcc/L21 high-entropy alloy: experiments and analytical modeling, Acta Mater. 262 (2024) 119426, https://doi.org/10.1016/j.actamat.2023.119426.

[16] Y. Wang, C. Huang, X. Ma, J. Zhao, F. Guo, X. Fang, Y. Zhu, Y. Wei, The optimum grain size for strength-ductility combination in metals, Int. J. Plast. 164 (2023) 103574, https://doi.org/10.1016/J.IJPLAS.2023.103574.

[17] K. Lu, A. Chauhan, F. Knöpfle, J. Aktaa, Effective and back stresses evolution upon cycling a high-entropy alloy, Mater Res Lett 10 (2022) 369–376, https://doi.org/10.1080/21663831.2022.2054667.

[18] X. Jin, Y. Liang, L. Zhang, J. Bi, Y. Zhou, B. Li, Back stress strengthening dual-phase AlCoCr2FeNi2 high entropy alloy with outstanding tensile properties, Mater. Sci. Eng., A 745 (2019) 137–143, https://doi.org/10.1016/j.msea.2018.12.097.

[19] Y. Yin, Q. Tan, Q. Sun, W. Ren, J. Zhang, S. Liu, Y. Liu, M. Bermingham, H. Chen, M.X. Zhang, Heterogeneous lamella design to tune the mechanical behaviour of a new cost-effective compositionally complicated alloy, J. Mater. Sci. Technol. 96 (2022) 113–125, https://doi.org/10.1016/j.jmst.2021.03.083.

[20] C. Zhou, Z. Kou, K. Song, J. Gong, P. Liu, Q. Gao, X. Liu, X. Han, Z. Zhang, P. Ramasamy, L. Hu, J. Orava, J. Eckert, Evading strength-ductility trade-off dilemma in TRIP-assisted Fe50Mn30Co10Cr10 duplex high-entropy alloys via flash annealing and deep cryogenic treatments, Acta Mater. 268 (2024) 119779, https://doi.org/10.1016/j.actamat.2024.119779.

[21] C.E. Slone, J. Miao, E.P. George, M.J. Mills, Achieving ultra-high strength and ductility in equiatomic CrCoNi with partially recrystallized microstructures, Acta Mater. 165 (2019) 496–507, https://doi.org/10.1016/j.actamat.2018.12.015.

[22] K. Lu, H. Shi, A. Weisenburger, J. Aktaa, Enhanced strength-ductility synergy of a partially recrystallized Al6Cr25Fe34Ni35 multi-principal element alloy, Mater. Char. 207 (2024) 113578, https://doi.org/10.1016/j.matchar.2023.113578.

[23] Y.W. Xiao, Z. Cheng, S.H. Li, S.Z. Wang, H.H. Wu, J.H. Gao, H.T. Zhao, F. B. Grumsen, G. Winther, G.L. Wu, X.P. Mao, O.V. Mishin, Recrystallization tuning to optimize mechanical properties in heavily rolled CoCrFeNi medium entropy alloy, J. Alloys Compd. 968 (2023) 172153, https://doi.org/10.1016/j.jallcom.2023.172153.

[24] M. Naeem, H. He, F. Zhang, H. Huang, S. Harjo, T. Kawasaki, B. Wang, S. Lan, Z. Wu, F. Wang, Y. Wu, Z. Lu, Z. Zhang, C.T. Liu, X.-L. Wang, Cooperative deformation in high-entropy alloys at ultralow temperatures, Sci. Adv. 6 (2024), https://doi.org/10.1126/sciadv.aax4002 eaax4002.

[25] D.D. Zhang, J.Y. Zhang, J. Kuang, G. Liu, J. Sun, Superior strength-ductility synergy and strain hardenability of Al/Ta co-doped NiCoCr twinned medium entropy alloy for cryogenic applications, Acta Mater. 220 (2021) 117288, https://doi.org/10.1016/j.actamat.2021.117288.

[26] K. Zhang, J. Chen, E. Zhang, R. Wei, S. Yuan, S. Zhang, Z. Han, C. Chen, T. Wang, F. Li, Strengthening of Fe50Mn25Ni10Cr15 medium-entropy alloys by Mo addition for cryogenic applications, Adv. Eng. Mater. 24 (2022), https://doi.org/10.1002/adem.202101363.

[27] Y. Wang, B. Liu, K. Yan, M. Wang, S. Kabra, Y.L. Chiu, D. Dye, P.D. Lee, Y. Liu, B. Cai, Probing deformation mechanisms of a FeCoCrNi high-entropy alloy at 293 and 77 K using in situ neutron diffraction, Acta Mater. 154 (2018) 79–89, https://doi.org/10.1016/j.actamat.2018.05.013.

[28] M.J. Jang, H. Kwak, Y.W. Lee, Y. Jeong, J. Choi, Y.H. Jo, W.M. Choi, H.J. Sung, E. Y. Yoon, S. Praveen, S. Lee, B.J. Lee, M.I. Abd El Aal, H.S. Kim, Plastic deformation behavior of 40Fe–25Ni–15Cr–10Co–10V high-entropy alloy for cryogenic applications, Met. Mater. Int. 25 (2019) 277–284, https://doi.org/10.1007/s12540-018-0184-6.

[29] Y.H. Jo, S. Jung, W.M. Choi, S.S. Sohn, H.S. Kim, B.J. Lee, N.J. Kim, S. Lee, Cryogenic strength improvement by utilizing room-temperature deformation twinning in a partially recrystallized VCrMnFeCoNi high-entropy alloy, Nat. Commun. 8 (2017) 1–8, https://doi.org/10.1038/ncomms15719.

[30] R. Zhang, S. Zhao, J. Ding, Y. Chong, T. Jia, C. Ophus, Short-range order and its impact on the CrCoNi medium-entropy alloy, Nature 581 (2020), https://doi.org/10.1038/s41586-020-2275-z.

[31] M. Saboktakin Rizi, H. Minouei, B.J. Lee, M.R. Toroghinejad, S.I. Hong, Effects of carbon and molybdenum on the nanostructural evolution and strength/ductility trade-off in Fe40Mn40Co10Cr10 high-entropy alloys, J. Alloys Compd. 911 (2022) 165108, https://doi.org/10.1016/j.jallcom.2022.165108.

[32] Z. Wu, W. Guo, K. Jin, J.D. Poplawsky, Y. Gao, H. Bei, Enhanced strength and ductility of a tungsten-doped CoCrNi medium-entropy alloy, J. Mater. Res. 33 (2018) 3301–3309, https://doi.org/10.1557/jmr.2018.247.

[33] S.H. Shim, J. Moon, H. Pouraliakbar, B.J. Lee, S.I. Hong, H.S. Kim, Toward excellent tensile properties of nitrogen-doped CoCrFeMnNi high-entropy alloy at

room and cryogenic temperatures, J. Alloys Compd. 897 (2022) 163217, https://doi.org/10.1016/j.jallcom.2021.163217.
[34] M.V. Klimova, D.G. Shaysultanov, S.V. Zherebtsov, N.D. Stepanov, Effect of second phase particles on mechanical properties and grain growth in a CoCrFeMnNi high entropy alloy, Mater. Sci. Eng. 748 (2019) 228–235, https://doi.org/10.1016/j.msea.2019.01.112.
[35] K. Jiang, B. Gan, J. Li, Q. Dou, T. Suo, Towards strength-ductility synergy in a CrCoNi solid solution alloy via nanotwins, Mater. Sci. Eng., A 816 (2021) 141298, https://doi.org/10.1016/j.msea.2021.141298.
[36] X. Wang, Y. Ding, Y. Gao, Y. Ma, J. Chen, B. Gan, Effect of grain refinement and twin structure on the strength and ductility of Inconel 625 alloy, Mater. Sci. Eng., A 823 (2021) 141739, https://doi.org/10.1016/j.msea.2021.141739.
[37] S.K. Guo, Z.L. Ma, G.H. Xia, X.Y. Li, Z.Q. Xu, W.Z. Li, X.Y. Jin, X.W. Cheng, Pursuing ultrastrong and ductile medium entropy alloys via architecting nanoprecipitates-enhanced hierarchical heterostructure, Acta Mater. 263 (2024) 119492, https://doi.org/10.1016/j.actamat.2023.119492.
[38] X. Wu, P. Jiang, L. Chen, F. Yuan, Y.T. Zhu, Extraordinary strain hardening by gradient structure, Proc. Natl. Acad. Sci. USA 111 (2014) 7197–7201, https://doi.org/10.1073/pnas.1324069111.
[39] S. Yoshida, T. Bhattacharjee, Y. Bai, N. Tsuji, Friction stress and Hall-Petch relationship in CoCrNi equi-atomic medium entropy alloy processed by severe plastic deformation and subsequent annealing, Scripta Mater. 134 (2017) 33–36, https://doi.org/10.1016/j.scriptamat.2017.02.042.
[40] S. Nag, W.A. Curtin, Acta Materialia Effect of solute-solute interactions on strengthening of random alloys from dilute to high entropy alloys, Acta Mater. 200 (2020) 659–673, https://doi.org/10.1016/j.actamat.2020.08.011.
[41] G. Bracq, M. Laurent-Brocq, C. Varvenne, L. Perrière, W.A. Curtin, J.M. Joubert, I. Guillot, Combining experiments and modeling to explore the solid solution strengthening of high and medium entropy alloys, Acta Mater. 177 (2019) 266–279, https://doi.org/10.1016/J.ACTAMAT.2019.06.050.
[42] B. Yin, F. Maresca, W.A. Curtin, Vanadium is an optimal element for strengthening in both fcc and bcc high-entropy alloys, Acta Mater. 188 (2020) 486–491, https://doi.org/10.1016/j.actamat.2020.01.062.
[43] B. Yin, W.A. Curtin, Origin of high strength in the CoCrFeNiPd high-entropy alloy, Mater Res Lett 8 (2020) 209–215, https://doi.org/10.1080/21663831.2020.1739156.
[44] W.G. Nöhring, W.A. Curtin, Correlation of microdistortions with misfit volumes in high entropy alloys, Scripta Mater. 168 (2019) 119–123, https://doi.org/10.1016/j.scriptamat.2019.04.012.
[45] C. Varvenne, A. Luque, W.A. Curtin, Theory of strengthening in fcc high entropy alloys, Acta Mater. 118 (2016) 164–176, https://doi.org/10.1016/j.actamat.2016.07.040.
[46] W.X. Zhang, Y.B. Cong, J. Wang, C. Li, J. Wan, Y.Z. Chen, Revealing the effects of martensitic transformation and dislocation slip in austenite on the micromechanical behaviors of a 9Ni steel using crystal plasticity finite element method, Int. J. Plast. 174 (2024) 103869, https://doi.org/10.1016/J.IJPLAS.2023.103869.
[47] C.A. Schuh, T.G. Nieh, H. Iwasaki, The effect of solid solution W additions on the mechanical properties of nanocrystalline Ni, Acta Mater. 51 (2003) 431–443, https://doi.org/10.1016/S1359-6454(02)00427-5.
[48] J.Y. He, H. Wang, H.L. Huang, X.D. Xu, M.W. Chen, Y. Wu, X.J. Liu, T.G. Nieh, K. An, Z.P. Lu, A precipitation-hardened high-entropy alloy with outstanding tensile properties, Acta Mater. 102 (2016) 187–196, https://doi.org/10.1016/j.actamat.2015.08.076.
[49] Z. Wu, H. Bei, G.M. Pharr, E.P. George, Temperature dependence of the mechanical properties of equiatomic solid solution alloys with face-centered cubic crystal structures, Acta Mater. 81 (2014) 428–441, https://doi.org/10.1016/j.actamat.2014.08.026.
[50] R.L. Fleischer, Substitutional solution hardening, Acta Metall. 11 (1963) 203–209, https://doi.org/10.1016/0001-6160(63)90213-X.
[51] S. Gao, X. He, Z. Tang, Q. Li, Z. Liu, W. Dong, Precipitation behavior and mechanical property evolution in a solid solution strengthened Ni-Cr-W superalloy during short-term aging, J. Alloys Compd. 981 (2024), https://doi.org/10.1016/j.jallcom.2024.173678.
[52] C. Chu, W. Chen, Z. Fu, L. Huang, H. Wang, D. Zhu, Realizing good combinations of strength-ductility and corrosion resistance in a Co-free Fe4Ni4Mn2CrTi high-entropy alloy via tailoring Ni/Ti-rich precipitates and heterogeneous structure, Mater. Sci. Eng., A 878 (2023) 145223, https://doi.org/10.1016/j.msea.2023.145223.
[53] J. Shen, W. Zhang, J.G. Lopes, Y. Pei, Z. Zeng, E. Maawad, N. Schell, A.C. Baptista, R.S. Mishra, J.P. Oliveira, Evolution of microstructure and deformation mechanisms in a metastable Fe42Mn28Co10Cr15Si5 high entropy alloy: a combined in-situ synchrotron X-ray diffraction and EBSD analysis, Mater. Des. (2024) 112662, https://doi.org/10.1016/J.MATDES.2024.112662.
[54] M. Yang, Y. Pan, F. Yuan, Y. Zhu, X. Wu, Back stress strengthening and strain hardening in gradient structure, Mater Res Lett 4 (2016) 145–151, https://doi.org/10.1080/21663831.2016.1153004.
[55] C.L. Chu, W.P. Chen, J.C. Liu, Q. Chen, Z.Q. Fu, Achieving strength–ductility synergy in a non-equiatomic Cr10Co30Fe30Ni30 high-entropy alloy with heterogeneous grain structures, Rare Met. 41 (2022) 2864–2876, https://doi.org/10.1007/s12598-022-02019-9.
[56] L. Tang, L. Wang, M. Wang, H. Liu, S. Kabra, Y. Chiu, B. Cai, Synergistic deformation pathways in a TWIP steel at cryogenic temperatures: in situ neutron diffraction, Acta Mater. 200 (2020) 943–958, https://doi.org/10.1016/j.actamat.2020.09.075.
[57] D.T. Pierce, J.A. Jiménez, J. Bentley, D. Raabe, J.E. Wittig, The influence of stacking fault energy on the microstructural and strain-hardening evolution of Fe-Mn-Al-Si steels during tensile deformation, Acta Mater. 100 (2015) 178–190, https://doi.org/10.1016/j.actamat.2015.08.030.
[58] Z. An, S. Mao, Y. Liu, L. Yang, A. Vayyala, X. Wei, C. Liu, C. Shi, H. Jin, C. Liu, J. Zhang, Z. Zhang, X. Han, Inherent and multiple strain hardening imparting synergistic ultrahigh strength and ductility in a low stacking faulted heterogeneous high-entropy alloy, Acta Mater. 243 (2023) 118516, https://doi.org/10.1016/j.actamat.2022.118516.
[59] T.S. Byun, On the stress dependence of partial dislocation separation and deformation microstructure in austenitic stainless steels, Acta Mater. 51 (2003) 3063–3071, https://doi.org/10.1016/S1359-6454(03)00117-4.
[60] G. Laplanche, A. Kostka, C. Reinhart, J. Hunfeld, G. Eggeler, E.P. George, Reasons for the superior mechanical properties of medium-entropy CrCoNi compared to high-entropy CrMnFeCoNi, Acta Mater. 128 (2017) 292–303, https://doi.org/10.1016/j.actamat.2017.02.036.
[61] S.J. Sun, Y.Z. Tian, H.R. Lin, H.J. Yang, X.G. Dong, Y.H. Wang, Z.F. Zhang, Transition of twinning behavior in CoCrFeMnNi high entropy alloy with grain refinement, Mater. Sci. Eng. 712 (2018) 603–607, https://doi.org/10.1016/j.msea.2017.12.022.
[62] Y. Zhao, Z. Chen, K. Yan, S. Naseem, W. Le, H. Zhang, W. Lu, An investigation on the microstructure and mechanical properties of Al0.3CoCrFeNi high entropy alloy with a heterogeneous microstructure, Mater. Sci. Eng., A 838 (2022), https://doi.org/10.1016/j.msea.2022.142759.
[63] L. Zhang, Z. Hu, L. Zhang, H. Wang, J. Li, Z. Li, J. Yu, B. Wu, Enhancing the strength-ductility trade-off in a NiCoCr-based medium-entropy alloy with the synergetic effect of ultra fine precipitates, stacking faults, dislocation locks and twins, Scripta Mater. 211 (2022) 114497, https://doi.org/10.1016/J.SCRIPTAMAT.2021.114497.
[64] H. Pouraliakbar, S.H. Shim, Y.K. Kim, M.S. Rizi, H. Noh, S.I. Hong, Microstructure evolution and mechanical properties of (CoCrNi)90(AlTiZr)5(CuFeMo)5 multicomponent alloy: a pathway through multicomponent alloys toward new superalloys, J. Alloys Compd. 860 (2021) 158412, https://doi.org/10.1016/j.jallcom.2020.158412.
[65] M.S. Rizi, H. Minouei, B.J. Lee, H. Pouraliakbar, M.R. Toroghinejad, S.I. Hong, Data supporting the hierarchically activated deformation mechanisms to form ultra-fine grain microstructure in carbon containing FeMnCoCr twinning induced plasticity high entropy alloy, Data Brief 42 (2022) 108052, https://doi.org/10.1016/j.dib.2022.108052.